Optimization and design of a novel small-scale integrated vacuum membrane distillation - solar flat-plate collector module with heat recovery strategy through heat pumps

Qiuming Ma, Aras Ahmadi, Corinne Cabassud

Optimization and design of a novel small-scale integrated vacuum membrane distillation - solar flat-plate collector module with heat recovery strategy through heat pumps

Qiuming Ma[a], Aras Ahmadi[a], Corinne Cabassud[a,*]

[a] TBI, Université de Toulouse, CNRS, INRA, INSA, Toulouse, France

[*] Corresponding author:

Corinne Cabassud

INSA Toulouse, TBI

135 Avenue de Rangueil

F-31077 CEDEX 4, Toulouse, France

Tel.: +33 5 61559782. E-mail: corinne.cabassud@insa-toulouse.fr

Abstract

This work aims to design a small-scale desalination unit for producing drinking water in remote places (~ 2L/person). It considers an equipment where vacuum membrane distillation (VMD) and direct solar heating through solar flat-plate collector (FPC) are coupled within the same intensified module, with photovoltaic (PV) panels providing electricity. An adapted heat pumping strategy is conceived to bridge between the heat-demanding feed recirculation and the heat-releasing vapor condensation, aiming both to recover latent heat of evaporation and to condensate without using an additional intensive cooling system. Sensitivity analyses and multi-objective optimizations are provided, based on water production and electric consumption of both pumping and cooling, to orientate the design and to discuss the key issues for an optimal operation. Results reveal that for a tiny module (0.18 m^2), a daily freshwater production of 3.7 L can be obtained with an average electric consumption of 17 W (~ 0.13 m^2 PV). At a relatively bigger scale (3 m^2), 96 L of freshwater is attained at a consumption of 449 W (~ 3.26 m^2 PV). The need for PV power capacity per unit water production is almost constant, ranging in 4.2 - 5 W L^{-1}.

Abbreviations: AGMD, Air gap membrane distillation; AMOEA-MAP, Archive-based multi-objective evolutionary algorithm with memory-based adaptive partitioning of search space; CP, circulation pump; CPC, Compound parabolic collector; DCMD, Direct contact membrane distillation; DMI, Delta moment-independent measure; ETC, Evacuated tube collector; FPC, Flat-plate collector; HR, Heat recovery; SEEC or electric SEC, Specific electric energy consumption; SGMD, Sweeping gas membrane distillation; SGSP, Salinity gradient solar pond; STEC or thermal SEC, Specific thermal energy consumption; VMD, Vacuum membrane distillation; VP, vacuum pump

Keywords

Vacuum membrane distillation; direct solar heating; heat pump; integrated module; remote places

Notations

A	Surface area, m^2
C	Salt concentration, g L^{-1}
c_p	Heat capacity of seawater, J kg^{-1} °C^{-1}
D	Distillate production, L
D_{s-w}	Diffusion coefficient of the salt in the seawater, m^2 s^{-1}
E	Electricity consumption, kWh
F_V	Volumetric flow rate, m^3 s^{-1}
h	Enthalpy, J kg^{-1}
ΔH	Latent heat, J kg^{-1}
J	Permeate flux, kg m^{-2} s^{-1}
K	Extinction coefficient, m^{-1}
K_m	Knudsen permeability of the membrane, s $mol^{1/2}$ m^{-1} $kg^{-1/2}$
L	Length of the module, m
M	Molar mass, kg mol^{-1}
m	Total mass of the feed, kg
$\dot{m}$	Mass flow rate, kg s^{-1}
n	Refractive index
P	Pressure, Pa
$\dot{P}$	Power, W
$\dot{Q}$	Heat flow rate, W
R	Ideal gas constant, J mol^{-1} K^{-1}
T	Temperature, °C
U	Heat loss coefficient, W m^{-2} °C^{-1}
V	Total volume of the feed, m^3
v	Velocity, m s^{-1}
W	Width of the module, m
$\dot{W}$	Work rate, W

x	Molar fraction

Greek letters

α	Absorptance
β	Slope, °
γ	Azimuth angle, °
δ	Thickness, mm
ε	Emittance
η	Efficiency
λ	Thermal conductivity, W m^{-1} $°C^{-1}$
μ	Dynamic viscosity, Pa s
ρ	Density, kg m^{-3}
φ	Latitude, °

Subscripts

a	evaporator side of heat pump
amax	ambient maximum
amin	ambient minimum
ap	absorber-plate
atm	atmosphere
b	condenser side of heat pump
bo	bottom
c	cover
comp	compressor
cp	circulation pump
f	feed bulk
in	inlet
is	isentropic
l	liquid phase
m	membrane surface
n	normal direction

out	outlet
p	permeate side
r	refrigerant
ref	reference
s	seawater supply
sat	saturated
v	vapor
vp	vacuum pump
w	pure water

1 Introduction

1.1 Membrane distillation

Membrane distillation (MD) is an emerging technology for seawater desalination, applying a hydrophobic microporous membrane to hold saline water and other non-volatile substances on the feed side and serve as the liquid-vapor interface of water evaporation [1]. Water partial pressure difference between the two sides initiates and drives the vapor migration, which often requires a higher temperature on the feed side. When being applied to small-scale compact desalination facilities, MD prevails over commonly used thermal distillation technologies (Multi-Effect Distillation, MED; Multi-Stage Flash, MSF) due to the large interfacial area of membranes [2]. Compared to reverse osmosis (RO), which is a membrane-based desalination technology that takes about 60% of global desalination capacity [3], merits of MD are also plenty. First, a theoretical 100% salt rejection is expected [4]. Furthermore, much higher water recovery rate with non-pressurized process and treatment for high-salinity water can be realized because no limitation by the osmotic pressure exists as such in RO, avoiding pressurized operations and large amounts of discharged brine [5].

Based on the configuration of the water-collecting side, or the permeate side, four different MD types have been studied the most in the literature [6], i.e. Direct Contact MD (DCMD), Air Gap MD (AGMD), Vacuum MD (VMD), and Sweeping Gas MD (SGMD). Among different types, VMD has received a lot of attention based on its negligible conductive heat loss through the membrane due to the vacuum on the permeate side [7,8], as well as a relatively higher and

controllable permeate flux [9]. Certain challenges have been deterring all kinds of MD from commercialization, including wettability of the membrane, scaling and fouling on the membrane surface and, more importantly, the enormous demand of thermal energy [10,11]. Despite this barrier, the relatively low working temperature (lower than 80 °C) [12] offers the possibility to equip MD with low-grade renewable energy resources, such as solar energy and waste heat, enhancing the overall thermal energy efficiency. In this paper, solar energy is selected as the solution to boost the competence of MD for seawater desalination in small domestic scale in remote areas, based on its availability all across the globe and its abundance especially in arid places where fresh water resource is deficient.

1.2 Solar energy in small-scale membrane distillation

Photovoltaic (PV) cells, as today's main solar-electricity conversion approach, can be installed to cover the electricity demand of MD systems. The installed capacity of photovoltaic panels can be directly adjusted according to the electrical need for pumps and other facilities. Furthermore, this electric demand is usually much lower compared to the thermal demand for phase change (667 kWh m^{-3} [11]) in MD. Therefore, most of the reported work in the literature has been focused on the efficient utilization of solar thermal energy for MD. Among all solar thermal collecting systems, Solar Collectors (SC), including Flat-Plate Collectors (FPC) and Evacuated-Tube Collectors (ETC), have been the most adopted types of solar energy collecting unit for the heat provision for MD process because of their relative high efficiency [13] and market availability.

Historically, theoretical modeling and simulations of small solar-driven MD systems have been an important approach to evaluate the feasibility and possible performance. Hogan et al. were among the very first practitioners to feed MD systems with solar heated saline water [14]. In their work, a hollow fiber DCMD module was coupled to solar FPCs with heat recovery in the system loop. Similar work was also carried out for flat-sheet DCMD modules [15], pointing out the importance of heat recovery to improve productivity and thermal efficiency when the amount of thermal energy brought in by solar energy is limited by the solar collector area. More recently, a small-scale FPC-driven DCMD system [16], an AGMD module with internal heat recovery [17], and a small SGMD desalination system coupled with solar collectors and PV panels but without latent heat recovery [18] have been theoretically studied as well. Experimental efforts have been

witnessed as well. Small-scale stand-alone AGMD units driven by solar energy was designed, manufactured and tested under the project "SMADES" [19,20]. Besides, DCMD [21,22] and VMD [23,24] with different membrane arrangements (flat-sheet [24], hollow fiber [21,23] and tubular [22]) have also been experimentally investigated. The interest of heat recovery was particularly evaluated in [21], where arranging heat exchange between the permeate and the feed allowed increasing the daily average water production by 37% and decreasing the specific energy consumption (SEC) by 31%.

Table 1: Data of reviewed research on small-scale solar-driven MD

MD study	SC Type	Latent heat recovery	SC area (m^2)	Membrane area (m^2)	Daily production (L)	SEC (kWh m^{-3})	Year
DCMD Simulation	FPC/ETC	External HE	3	1.8	50	42.7 - 556* (thermal)	1991 [14]
AGMD Experiment	FPC	Internal condensation	5.73	10	120	200 - 300 (thermal)	2007 [19]
AGMD Experiment	FPC	Internal condensation	5.73	N/A	64	647* (thermal)	2008 [20]
VMD Experiment	N/A	-	8	0.09	15.6*	7858*(thermal) + 317*(electrical)	2009 [23]
AGMD Experiment/ Simulation	N/A	Internal condensation	0.07*	0.05	0.2 - 0.25	N/A	2012 [17]
VMD Experiment	ETC	-	2.16	0.25	3	750 (thermal)	2014 [24]
DCMD Experiment	FPC	External HE	20	3.39	No HR: 18.4* HR: 25.2*	No HR: 2342 HR: 1609 (thermal)	2015 [21]
DCMD Experiment	ETC	-	2.61*	1	26.76 - 33.55	N/A	2017 [22]
DCMD Simulation	FPC	-	22.6	7.2	140	N/A	2017 [16]
SGMD Simulation	FPC	-	27 + 4 (PV)	1.03	240	N/A	2018 [18]

N/A: Not available in the reference

HE: Heat Exchanger; HR: Heat Recovery

*: Calculated or estimated from data and figures in the corresponding paper

In order to have a panorama of the above-mentioned work, the MD study type, SC type, heat recovery approach, system scale (surface area of SC and membrane), daily production, SEC (both thermal and electrical, the latter being rarely provided), and corresponding reference are listed in Table 1.

Apart from the typical SC-driven MD with separated SC and MD modules, some integrated modules combining MD and SC directly into one small equipment have been emerging since about a decade ago, aiming more intensified process, more compact system adapted to small-scale distributed applications and less pressure and heat loss due to piping and heat exchanging. A hybrid solar distillatory, combining flat-sheet AGMD with a conventional basin still [25], was one of the earliest practice of this idea. Experiments and numerical simulations revealed that the daily distillate productivity was only 2.18 kg m^{-2} day^{-1}, and the calculated STEC was as high as 2880 kWh m^{-3}. Started from 2010, both experimental and modeling efforts were made for DCMD [26] and for AGMD [27,28], using the space for water circulation under the absorber-plate as the MD module with feed side being heated by solar radiation. However, the modules were not considered as an independent desalination system, and the dynamic performance with varying solar condition and accumulated water production were not studied. In 2011, Mericq et al. [10] conducted a series of indicative simulations on integrated solar-VMD modules and separated VMD modules with solar collecting unit. Inspired by this preliminary results, a detailed modeling and simulation approach was developed by Ma et al. [29] with comprehensive dynamic analysis on the parameters and the overall performance, resulting in a daily production of 8 L m^{-2}. Hollow fiber VMD modules were also studied with this integration idea by being inserted into the cylindrical absorber of CPC solar collectors [30], which offered the possibility of directly absorbing intensified solar radiation for fresh water production to overcome the sparsity of solar energy. Most recently, a delicately fabricated VMD-ETC module was studied via simulation and experiment [31]. Hollow fibers membranes of 0.2 m^2 were inserted into the ETC tubes with a total solar absorbing area of 1.6 m^2. 3.2 ~ 4.8 L of drinking water and a certain amount of bath water at 45°C could be produced on a daily basis, at a cost of 1 kWh electricity and 4.7 - 9.6 kWh solar exposure.

1.3 Literature gap and research objective

All the daily distillate productions reviewed above hardly reached 10 L m^{-2} in terms of the total surface area of SC and membrane, and the value was even lower if heat recovery was excluded. This productivity was relatively low compared with the permeate flux of conventional MD systems with continuous auxiliary heating source (~ 10 L m^{-2} h^{-1}), which suggests that the amount of solar energy supply is a limitation [29]. On the other hand, much higher consumption was encountered if heat recovery was not considered, on account that the demand of latent heat for water evaporation is rather important, being around 667 kWh m^{-3} [11]. Conclusively, an efficient latent heat recovery regime is of great interest to surmount the obstacle of the restricted solar energy supply, and to achieve significant improvement in both water productivity and energy consumption [32]. However, little work has been seen towards the latent heat recovery design in VMD research, even though VMD possesses the merits of low thermal loss and high productivity. The reason is probably due to the low condensation temperature in vacuum environment, which induces great difficulty of reusing latent heat. Another overall observation throughout the literature is, the majority was focused on the thermal energy consumption of the solar-driven MD system without specifying the electric expense. Moreover, nearly no study on energy consumption has included the discussion of extra cooling energy requirements for permeate condensation, which would be significant if the condenser is placed in the vacuum of VMD.

Based on the observations above, a heat pump might fit just well for the heat recovery in VMD, transporting heat from the low-temperature permeate condensation to the high-temperature feed circulation. Furthermore, the multi-functionality of the heat pump in both permeate cooling and feed heating ensures the system performance analysis to be more comprehensive, including the consideration of cooling consumption. Following the previous work, where a directly integrated VMD-FPC module was designed and studied [29], a recirculation system is conceived and further enhanced by a practical strategy for the simultaneous heat recovery and permeate condensation via a heat pump in the present study, targeting a small and compact desalination module for remote coastal areas or isolated islands. In addition, this work provides global sensitivity analyses and fast design-oriented multi-objective optimizations, in order to orientate

the design and to globally optimize the most influential parameters among solar-heating concerned parameters, membrane permeability, operating conditions and module dimensions, as well as to discuss the key issues for an optimal functioning of the whole process.

2 Process description and modeling: coupled VMD-FPC with integrated heat pump

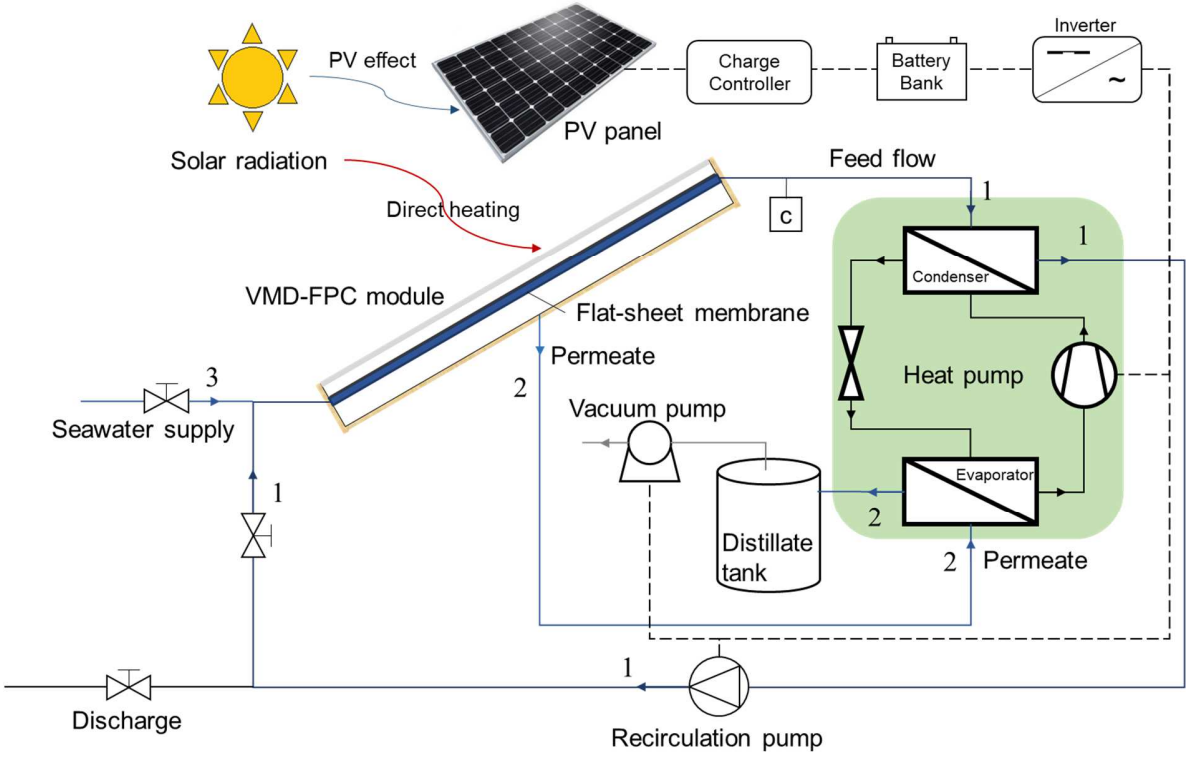

Figure 1: Flowsheet of VMD-FPC recycle system with integrated heat recovery by heat pump

The flowsheet for the entire system including the VMD-FPC module, heat pump and recirculation system is illustrated in Figure 1. One important specificity of the present VMD-FPC module is that it admits the same surface for solar collector and membrane. Seawater is supplied (Stream 3) through the feed side and then recycled via the recirculation pump (Stream 1) by passing also through a heat pump (in light green block). The flow rate of the seawater supply (Stream 3) is at each time equal to the permeate flow rate (Stream 2), in order to provide a constant recirculation flow at the membrane feed side. If no wetting and no operational failure of the VMD process occurs during the operation, the salt concentration of the feed (Stream 1) keeps accumulating. When the highest tolerable concentration (a setting of 300 g L^{-1} was currently selected in this work [33], and it can be further determined by future experimental tests on scaling

and fouling risks) is detected by the concentration meter “c” at the outlet of the module, the whole operation stops and the system is evacuated by the discharge and then refilled through the seawater supply (Stream 3) in Figure 1. Finally, a photovoltaic (PV) system with an appropriate capacity, according to the simulation result of the electric consumption, has to be installed to provide electricity for the vacuum pump, the recirculation pump and the compressor. It normally includes a PV panel, a charge controller, a battery bank and a DC-AC inverter.

The vacuum pump is the key element to maintain the low pressure on the permeate side and to allow for a considerable permeation even at low feed temperatures. The permeate is cooled and condensed in contact with the cold source of the heat pump and then transported to be collected in the distillation tank (Stream 2). The heat pump block (in light green) in Figure 1 allows the energy transfer from the cold source (Evaporator) to the hot source (Condenser) by using an intermediate compressor. In this fashion, the latent heat of evaporation is taken from the permeate (Stream 2) at the cold source and recovered back to the hot source to heat the recirculation flow (Stream 1). Besides, compared to the placement of the vacuum pump in the previous work where all the permeate vapor was compressed by the vacuum pump and then condensed [29], here in this configuration the energy consumption is expected to be much lower due to the smaller amount of vapor to be pumped out by vacuum pump. Summarily, connecting the permeate condensation before the vacuum pump and the heating of the feed side through a heat pump is potentially of great interest in the context of VMD modules, because it allows the simultaneous achievement of the two following goals: (i) ensuring an efficient permeate condensation under vacuum pressure with no extra intensive cooling utilities and lower electricity need for the vacuum pump, (ii) ensuring a relevant degree of heat recovery from permeate condensation.

Following the overall flowsheet, the VMD-FPC module and the heat pump are respectively described in Section 2.1 and 2.2, and the integrated modeling structure of the whole system with its dynamics is presented in Section 2.3. Besides, the detail on heat pump calculation is in Appendix A in the supplementary material.

2.1 Coupled solar flat-plate vacuum membrane distillation collector

The configuration of the integrated VMD-FPC module [29] is shown in Figure 2, which is similar to the configuration in [26,28] for DCMD and AGMD. The present design imposes few modifications to the structure of a normal FPC and also benefits from the high absorption capacity of the absorber-plate in commercially available FPCs. The MD module is inserted into the water circulation space under the absorber-plate (Figure 2), sharing the same surface with the solar collector. The glazing glass cover allows solar radiation to penetrate, which is then absorbed by the absorber-plate and heats up the feed side. Identical to a solar collector, the entire module is enclosed by a thermal insulation material.

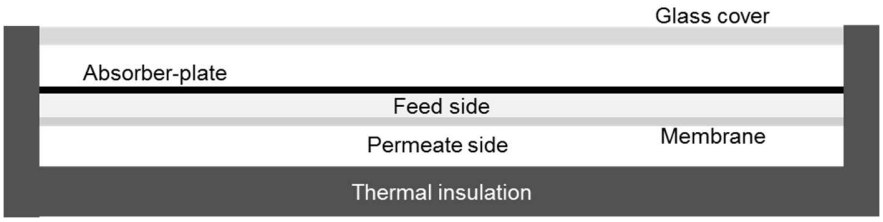

Figure 2: Cross-sectional view of integrated FPC-VMD module

Solar radiation model was mainly adapted and developed from Duffie and Beckman [34], and was explained in detail in [29]. It is location and time sensitive and cloudiness has not yet been taken into account. Isotropic diffuse model was assumed and the final absorbed solar energy was modeled from the ultimate source, the sun, to the absorber-plate step-by-step. The final utilized solar energy was obtained from the absorbed energy deducted by the thermal loss to the ambient, which is subject to the coupled VMD model.

The membrane pore model had previously been developed and validated [5], with the description of the permeate flux, as well as the temperature and concentration polarization. The main assumptions taken into consideration were (i) the evaporation only occurring at the pore entrances where the liquid-vapor interface was located; (ii) the absence of wetting, fouling or crystallization throughout the process, thus no salt penetrating the membrane; (iii) Knudsen diffusion only (collisions of vapor molecules with the pore wall) [35] determining the mass transfer through the pores of the membrane; (iv) neglecting the transmembrane conductive heat loss and the boundary layer on the permeate side, due to the vacuum and the total vapor phase in the permeate compartment [33]; (v) the properties of seawater calculated from its activity

coefficient γ_f and its water molar fraction x_w obtained using the PHREEQC software (version 2.13.1, US Geological Survey) [36].

The feed bulk longitudinal model further aggregates the above models by a series of ordinary differential equations to predict the profiles of hydraulic pressure, temperature, flow velocity and salt concentration along the feed flow direction. The solar radiation calculation was coupled to it through the modeling of the utilized solar energy intensity, and the membrane pore model was coupled to it by the local permeate flux.

2.2 Heat recovery from condensation by heat pump

The structure of the heat pump is shown in Figure 3. This structure should be seen as an illustrating attempt for feasibility check, based on a single-stage heat pump. The refrigerant is used to condense the permeate vapor at the cold source (Heat pump evaporator in Figure 3) by absorbing the latent heat of water evaporation and to return it to the feed circulation at the hot source (Heat pump condenser in Figure 3). Therefore, the refrigerant should be capable of working between a low-temperature level (preferably below 0°C) to maximize the condensation of the permeate vapor under vacuum, and a certain temperature level to pass some heat back to the feed recirculation. The two heat exchangers (Evaporator and Condenser in Figure 3) are the only contact points between the heat pump and the MD system.

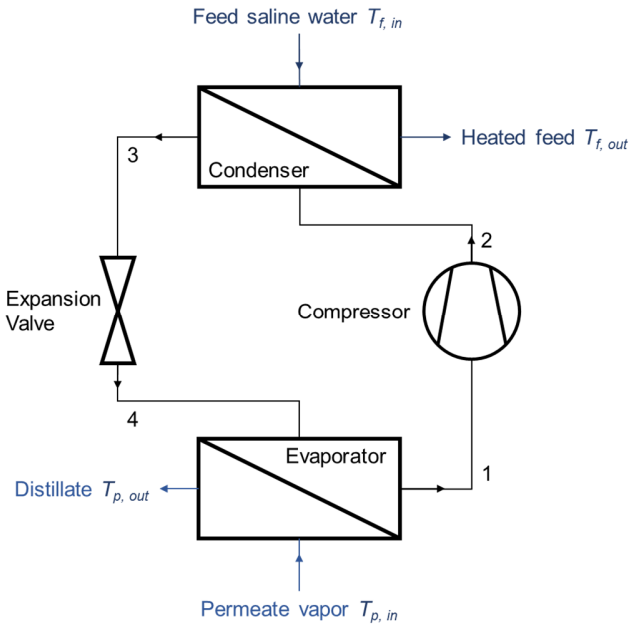

Figure 3: Configuration of interconnected heat pump and VMD system

As illustrated in Figure 3, the permeate vapor is condensed in the evaporator, passing the heat of water evaporation to the low-temperature and low-pressure refrigerant which evaporates to Point 1. Then the vapor is taken to relatively higher temperatures and pressures at Point 2 by a compressor and led to the condenser, where the feed saline water flows on the other side of the heat exchanger and can be heated if its temperature is below the dew point of the refrigerant. On the other hand, the refrigerant is condensed, then subcooled by the heat transfer to the feed flow (feed saline water in Figure 3). Afterward, it experiences an expansion through the expansion valve, back to Point 4. Finally, the cold refrigerant reaches the evaporator, where its low temperature ensures again the permeate condensation.

Oppositely to the previous work [29], here the permeate condensation takes place mostly before the vacuum pump, via an effective heat exchange with the evaporator of the heat pump. Along with the assumption of a heat exchange efficiency η_a, only a small proportion of the permeate vapor has to be pumped out by the vacuum pump, in contrast with the configuration where all the permeate vapor being pumped out by the vacuum pump. Consequently, the burden of the vacuum pump in this study is much diminished.

Broadly speaking, an effective permeate condensation under vacuum in a VMD system, such as the case in the current study, demands intensive cooling facilities. However, its integration and consumption in the system have seldom been taken into account. Instead, in the current study, the low evaporating temperature of -2°C of the refrigerant in the heat pump guarantees the effective vapor condensation, whose consumption is included in the compressor work in the heat pump.

2.3 Modeling structure, recirculation and system dynamics

Figure 4 provides the structure of models involved in the present work. In the center of the structure, the model for recirculation and system dynamics is placed as the global combing node. At this level and regarding the process flowsheet in Figure 1, the dynamics are included based on time-varying steady-state phases [29].

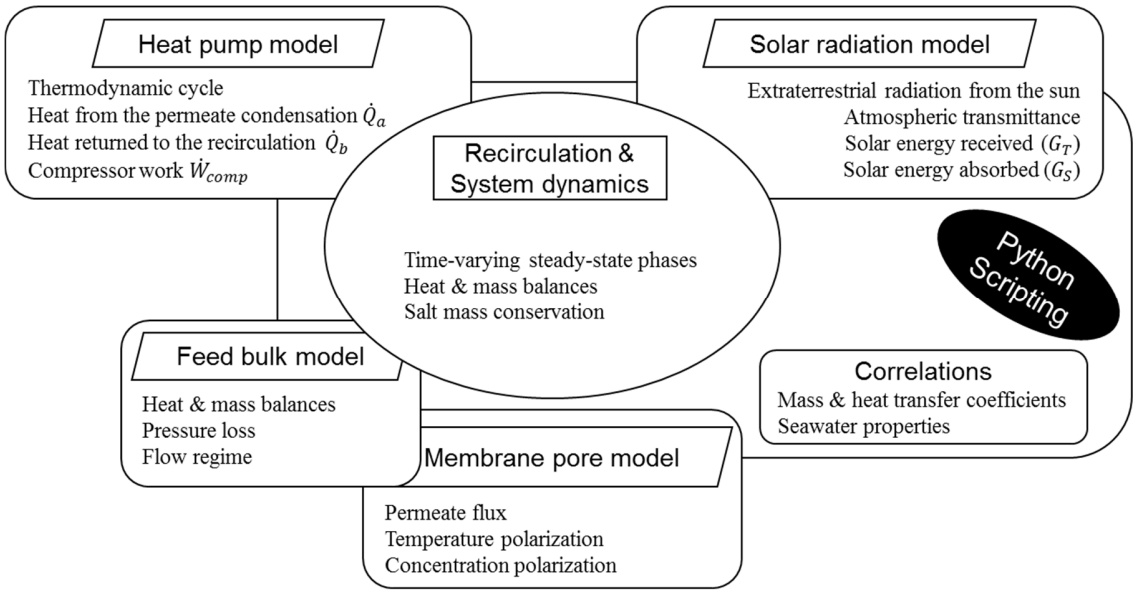

Figure 4: Schematic of modeling process

As given in Eq. 1, the total mass (m) is assumed to be maintained constant by a continuous compensation ($\dot{m}_s$) through seawater supply for water permeation ($\dot{m}_p = J_w A_c$, with J_w the permeate flux and A_c the total area of the module). On the other hand, the concentration accumulation rate in the VMD-FPC module can be described by the incoming rate of salt mass from water supply $\dot{m}_s$ (concentration C_s, density ρ_s), formulated in Eq. 2 with V being the total volume of the module feed side. Finally, the temperature variation on the feed side is determined

by the sum of the recovered heat from the condenser of the heat pump $\dot{Q}_b$, the utilized solar energy power $G_u A_c$ and the energy carried by the incoming water supply, as well as the outgoing permeate with both sensible and latent heat, as shown in Eq. 3. Therefore, the feed temperature is determined dynamically during the operation, not fixed as an inlet operating parameter.

$$\frac{dm}{dt} = \dot{m}_s - \dot{m}_p = 0 \tag{1}$$

$$\frac{dc}{dt} = \frac{1}{V}\left(\frac{\dot{m}_s c_s}{\rho_s}\right) \tag{2}$$

$$\frac{d\left(c_p m T_f\right)}{dt} = \dot{Q}_b + G_u A_c + \dot{m}_s h_s - \dot{m}_p\left(h_p + \Delta H_{w,v}\right) \tag{3}$$

A comprehensive model for the VMD-FPC module has been built with coupled VMD model and Solar radiation model, both of which have been validated previously in [29]. As it is illustrated in Figure 4, the above-mentioned VMD-FPC model involved:

- Membrane pore model, admitting Knudsen diffusion, temperature and concentration polarization in order to locally determine temperature and concentration as well as the permeate vapor flux at the membrane surface;

- Feed bulk model, establishing longitudinal properties along the feed side of the module (this includes mass and heat balances and momentum equation);

- Mass and heat transfer coefficients: the convective heat transfer coefficient for the heat transfer from feed bulk to the membrane surface from Nusselt number (Nu) correlations in the rectangular channels for laminar regime [37] and transitional or turbulent regime [38], the mass transfer coefficient for the salt diffusion from feed bulk to membrane surface from semi-empirical correlations using Sherwood number (Sh) and Schmidt number (Sc) [39];

- Seawater properties: dynamic viscosity μ, density ρ and thermal conductivity λ from the regressions in [36], heat capacity of the seawater is taken from [40], and the diffusion

coefficient of the salt in the seawater D_{s-w} from Stokes-Einstein relation with salt being assimilated as NaCl [41];

- Solar radiation model, determining the solar energy utilized (G_u) involving the estimation of solar radiation on the ground based on isotropic sky model where transmission, reflection, and absorption of radiation are included and referred to as functions of incoming radiations and main properties of the solar collector [29].

Same solution procedure as the previous work was adopted [29]. First, a system of differential-algebraic equations (DAEs) was resolved by the feed bulk longitudinal profile discretized along the module length and the set of algebraic equations describing the process in membrane pores. Then, Scipy ODE package with the Real-valued Variable-coefficient Ordinary Differential Equation solver (Isoda) [42] was applied to automatically process the system dynamics Eq. 1-3. It should be noted that all models in the present work were programmed in Python (version 2.7.11).

3 Performance assessment and analysis

3.1 Decision variables, design parameters and performance indicators

Overall, 15 decision variables were involved with reasonable value ranges for each one (Table 2), including module dimensions, solar collector properties, permeability of the membrane and operating conditions. All the ranges of these variables are either limited by practical operating conditions or by realistic properties of the material. The last decision variable, the condenser efficiency in the heat pump (η_b), is particularly important because it directly determines the heat recovery level when heat pump is running. η_b was limited between 0, which means no heat recovery from the condenser of heat pump to the feed, and 0.8.

Table 2: Decision variables for VMD-FPC module with heat pump

Variable	Range	Description
n_c	1.2 ~ 1.8	Refractive index of the cover
K	4 ~ 32	Extinction coefficient of the cover, m^{-1}
δ_c	2 ~ 5	Thickness of the transparent cover, mm
ε_c	0.6 ~ 0.95	Emittance of the cover
ε_{ap}	0.1 ~ 0.95	Emittance of the absorber-plate

α_n	0.8 ~ 0.95	Absorptance in normal direction
β	0.0 ~ 70.0	Slope of the solar collector, °
γ	-40.0 ~ 40.0	Azimuth angle of the solar collector, °
W	0.1 ~ 1.5	Width of the collector, m
δ_f	0.5 ~ 30	Flow channel thickness, mm
L	0.1 ~ 2.0	Module length, m
K_{mref}	3.0×10^{-6} ~ 1.85×10^{-5}	Membrane Knudsen permeability at 20°C, s $mol^{1/2}$ m^{-1} $kg^{-1/2}$
Re	500 ~ 10000	Reynolds number at the inlet
P_p	650 ~ 20000	Vacuum pressure on the permeate side, Pa
η_b	0 ~ 0.8	Condenser efficiency in heat pump (When no heat recovery: $\eta_b = 0$)

On the other hand, for the fixed parameter settings in the simulations (detailed in Table 3), the evaporator efficiency in the heat pump (η_a) was assumed to be fixed at a constant high value (0.95), based on: i) the constant temperature difference between the refrigerant evaporation and the permeate vapor condensation; ii) the low evaporation temperature ensuring an effective vapor condensation to release the burden of the vacuum pump, as discussed in Section 2.2; iii) that the variation of heat recovery efficiency was already taken into consideration by the largely varying condenser efficiency. All simulations were conducted under the condition of a cloudless and sunny day from 8:00 in the morning to 20:00 in the evening (12 hours of daily operation) on 1st August at the location of Toulouse, in order to take an example of system operations and to give indications on the experimental tests here in the laboratory. Other fixed parameter settings are summarized in Table 3 as well.

Table 3: Parameter settings for VMD-FPC module with heat pump

Parameter	Value	Description
L_{loc}	358.56	Longitude in degrees west, $0° \leq L < 360°$
φ	43.60	Latitude, north positive, $-90° \leq \varphi \leq 90°$
A_{loc}	150.0	Altitude of the location, m
h_{wind}	10	Heat transfer coefficient of the wind, W m^{-2} $°C^{-1}$
r_0, r_1, r_k	0.97, 0.99, 1.02	Correction factors for mid-latitude summer [34]
ρ_g	0.2	Diffuse reflectance of the surroundings
T_{amax}	35	Highest ambient temperature, °C

T_{amin}	20	Lowest ambient temperature, °C
C_s	35	Salt concentration of the seawater supply, g L^{-1}
T_s	25	Temperature of the seawater supply, °C
C_{limit}	300	The highest operating salt concentration, g L^{-1}
U_{bo}	0.9	Heat loss coefficient of the insulation, W m^{-2} $°C^{-1}$
η_a	0.95	Evaporator efficiency in heat pump
η_{is}	0.8	Isentropic efficiency of the compressor in the heat pump

As regards the heat pump, the organic fluid Solkatherm (SES36) was selected to be the working medium as a first attempt of this work, based on the specificity of cooling and heating requirements identified and mentioned in Section 2.2. SES36 is an azeotropic mixture of Pentafluoropropane R365mfc/perfluoropolyether (65% - 35% by mass), well-known in power industry and in organic Rankine cycles. Recently, its application in case of low-temperature ORC systems for waste heat recovery application has been studied [43]. SES36 is not toxic, not flammable, no ozone depletion potential (ODP) and it is more environmentally friendly when compared with commonly used refrigerants such as R134a or R404a [44]. More importantly, the corresponding pressure difference between the condenser and evaporator of heat pump can be lowered if SES36 is applied instead of other common refrigerants, thanks to its thermodynamic properties when working between an evaporator temperature of -2°C and a certain condenser temperature. Consequently, the compressor work can be comparatively less demanding with SES36 being the working fluid, due to the lower pressure difference that needs to be created by the compressor of heat pump. The main operating conditions of the heat pump are listed in Appendix B in the supplementary material.

The main performance indicators for this VMD-FPC system are the distillate production D in kilogram during the 12-h operation, and the total energy consumption E in kWh, considering the aim of efficient fresh water production in small and distributed scale for low electricity consumption E, which further requires installed PV fields if a total autonomous operation is desired, as shown in Figure 1. The calculation of E is introduced in detail in Appendix C.

3.2 Sensitivity analysis via Delta Moment-Independent (DMI) indicator

The Sensitivity Analysis (SA) aims to comprehend how much the decision variables affect the problem's objectives. Then, the indications on how to ameliorate system performance can be achieved by specifying and analyzing the most influential variables from these results. Instead of a simple one-at-a-time (OAT) analysis [29], a global SA is envisioned in the present work. Here, the Delta Moment-Independent (DMI) indicator in SALib Python library [45] was selected, i.e. an approach with a global sensitivity index δ based on given data to identify the impact of each parameter at the minimum computational cost [46,47]. It is sampling-free and able to work on an already available set of data, and therefore, compatible with simultaneous coupling with optimization studies. The index δ represents the normalized expected shift in the distribution of the output provoked by fixing a certain input variable, which ranges in [0, 1] and equals 0 when the output is totally independent of the input variable in question [46]. Besides, the DMI package in Python also features a first-order variance-based sensitivity indicator S1 for each input variable, which represents the expected percentage reduction of the output variance when the variable is fixed [48]. Consequently, S1 is scaled in [0, 1] as well.

3.3 Fast multi-objective optimization on design and operating conditions

A multi-objective problem describes conflicting objectives, where improving one objective results in the deterioration of another. An unconstrained problem can be mathematically stated as,

$$\begin{aligned} &\text{Minimize} && f_i(x), \forall i \in \{2, \dots, m\} \\ &\text{Subject to} && x \in \mathrm{R}^n \end{aligned} \tag{4}$$

Where, m is the number of objectives, x the vector of decision variables, $f_i(x)$ the objective functions, and R^n the real space of n decision variables. The concept of domination is defined to discriminate solutions one against another. For two solutions x_1 and x_2, the solution x_1 is said to dominate x_2 if and only if $f_i(x_1) \leq f_i(x_2)$ for all objective functions and $f_i(x_1) < f_i(x_2)$ for at least one objective function. The Pareto front (PF) comprises all optimal solutions belonging to the set of non-dominated optimal solutions.

According to the present study, by taking $f_1 = (-\mathrm{D})$ and $f_2 = \mathrm{E}$ as the objective functions, a bi-objective optimization problem is formed, where as a result, energy consumption (E) is

minimized while water production (D) is maximized. The set of 15 decision variables is taken into account with their respective ranges, resulting in an intermediate problem dimension. Furthermore, the better choices of some of the decision variables will be discussed based on the optimization results.

For this bi-objective optimization problem, a Pareto front is expected to represent the set of alternative scenarios. However, the dynamic simulations together with interrelated modeling and resolutions, as discussed in Section 2.3, can be time-consuming. Thus, in order to reduce the computational budget as much as possible, the archive-based multi-objective evolutionary algorithm with memory-based adaptive partitioning of search space (AMOEA-MAP) was adopted as the fast optimization algorithm [49,50], which aims to provide an efficient and steady convergence over the Pareto front within a limited number of simulation runs. For the present study, the computational budget was limited to 3000, which means that overall, 3000 simulations were operated to form the optimal Pareto front.

It should also be noted that the heat recovery level is clearly an essential factor for both objectives in this study, as reported also in the literature [32]. Therefore, in order to better observe its influence on the overall performance, different heat recovery levels determined by fixed η_b = {0, 0.2, 0.4, 0.6, 0.8} were studied independently, yielding a 14-variable optimization for each case. Varying η_b was also taken into consideration to perform an additional optimization afterwards. For the sake of simplicity, a small reformulation was applied by merging the extinction coefficient K and the thickness δ_c of the glazing cover into a dimensionless product $K\delta_c$, which keeps the number of variables at 14. These two variables are mainly involved in the calculation of the radiation absorbed by the cover, which is determined by their product.

4 Results and discussions

4.1 Sensitivity analyses

4.1.1 Sensitivity variation due to heat recovery from permeate condensation

For a better view of the global change in sensitivities while operating under different heat recovery levels, the sensitivities of all decision variables were shown at two opposing regimes: without heat recovery ($\eta_b = 0$) and with maximum heat recovery from permeate condensation (η_b

= 0.8). Figure 5a, 5b show the results for no heat recovery and Figure 5c, 5d for maximum heat recovery.

With respect to the results provided in Figure 5, the two indicators (DMI and S1) more or less describe the same sensitivity trends. However, the S1 indicator clearly shows a larger discrepancy between more sensitive and less sensitive variables than the DMI. Besides, the distribution of all the sensitivities presents more or less the same situation in both objectives D (Figure 5a, 5c on the left) and E (Figure 5b, 5d on the right). The 3 most influential variables are always found to be the length L, the width W of the module (or the module surface area) and the vacuum pressure P_p of the permeate side, as expected for the VMD process. In the current module, the areas of both the solar absorbing surface and the flat-sheet membrane surface are quantified by $W \times L$. As a result, both the amount of thermal energy source and the water producing area of the distillation membrane are directly determined by these dimensions, giving the relatively high sensitivities of the objectives. As expected, P_p appears to be another influential variable, based on its predominance in VMD operation [29].

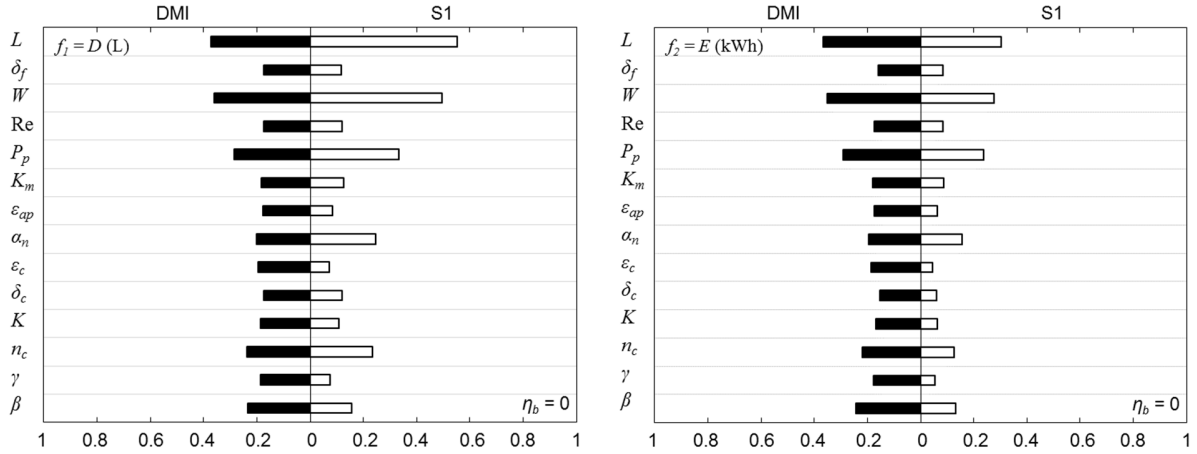

(a) (b)

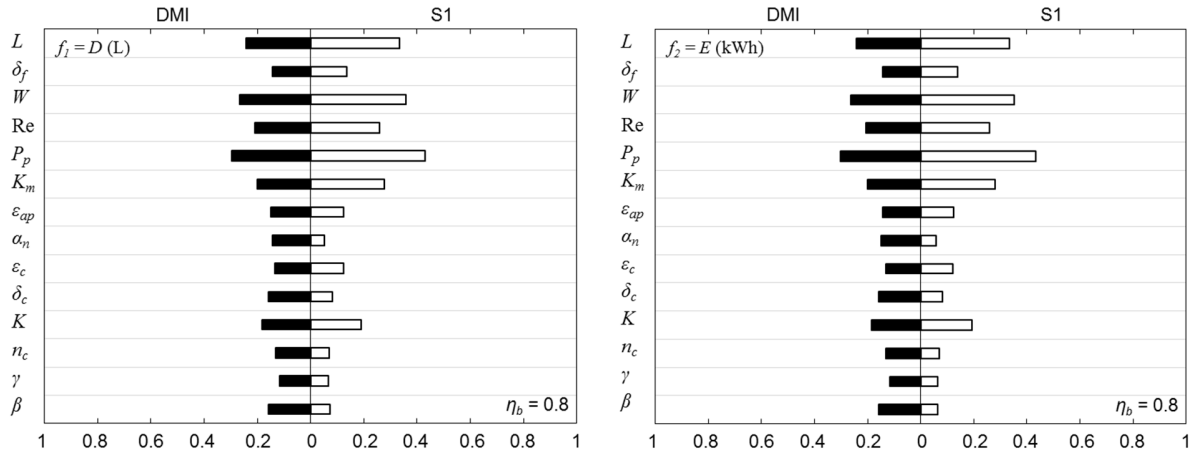

(c) (d)

Figure 5: DMI and S1 sensitivity indicators with respect to different variables: (a) study of water production D at no heat recovery regime (η_b = 0); (b) study of energy consumption E at no heat recovery regime (η_b = 0); (c) study of water production D at maximum heat recovery (η_b = 0.8); (d) study of energy consumption E at maximum heat recovery (η_b = 0.8)

Nevertheless, significant differences can be observed between the scenarios with and without condensation heat recovery. Overall, the solar energy-oriented variables, i.e. the bottom 8 variables in all graphics in Figure 5, show lower sensitivities for a module operating with heat recovery (Figure 5c, 5d) when compared with a system without heat recovery (Figure 5a, 5b). Especially for the global solar energy absorptance in the normal direction (α_n) and the inclination of the module (β), less significance was observed in the case where η_b = 0.8, because that the amount of solar energy available on the surface of the module was less important when the efficient heat recovery helped relieve the thermal demand. Moreover, in the case of heat recovery from condensation, the sensitivities were more distributed (taking the DMI as the sensitivity indicator, for example) and more particularly for the VMD process variables, namely the Knudsen permeability at the reference temperature (K_{mref}), Reynolds number of the feed flow and vacuum pressure P_p, they gained in weight, compared to a VMD-FPC module without heat recovery. In other words, the variables that mainly intervenes in the mass transfer of VMD became more important when a high heat recovery level was implemented, which is also comprehensible due to the higher attainable permeate production under the less restrained thermal energy source with the recovered heat.

549

550 *4.1.2 Importance of heat recovery level*

551 Performance at different levels of heat recovery is studied in this section by allowing η_b to vary
552 within [0, 0.9]. This was achieved practically by taking the condenser efficiency (η_b) of the heat
553 pump as a new variable, and merging the extinction coefficient K and the thickness δ_c of the
554 glazing cover into the dimensionless product $K\delta_c$ to consistently keep 14 variables, as mentioned
555 above. As a result, a new series of sensitivity analyses was performed, based on 3000 newly
556 generated operating points. The sensitivities of D and E were evaluated with 14 decision
557 variables, as shown in Figure 6, including η_b as the new operating variable.

558

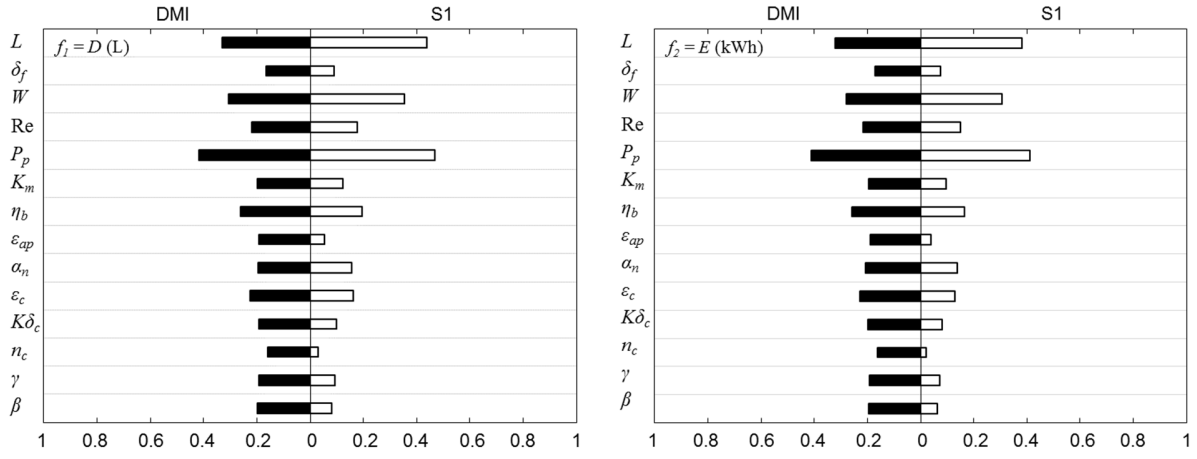

(a) (b)

559 Figure 6: DMI and S1 sensitivity indicators with respect to different variables: (a) study of water
560 production D; (b) study of energy consumption E at varying heat recovery level

561

562 As can be seen in Figure 6, DMI and S1 for all sensitivities show more or less the same shape,
563 but the sensitivities in DMI are more evenly distributed than those in S1. Then, the sensitivities to
564 the variables of the two different objectives (D and E) are similar to each other. These general
565 features highly resemble the cases in Figure 5. The varying η_b did not alter the 3 most important
566 variables in Figure 5, i.e. the length L, the width W of the module and the vacuum pressure P_p,
567 while it came as the 4th significant variable for both Figure 6a and 6b. However, if considering
568 an existing module with certain dimensions and a certain vacuum level, the efficiency of heat
569 recovery would be clearly of more importance than all the solar absorption-oriented variables and

VMD process variables. In other words, the factor of heat recovery would have a strong impact on the performance of a given VMD-FPC module.

4.2 Global optimization of module and performance improvement using heat pump

According to the problem formulation proposed in this work, significantly higher water production D and lower energy consumption E were targeted. Taking the heat recovery level as a new variable, as formulated and explained in Section 4.1.2, the whole system was optimized via the AMOEA-MAP algorithm with a budget of calculation of 3000 simulation runs. The ranges of variables have been defined in Table 2.

As a result, Figure 7a shows the non-dominated Pareto front, i.e. the set of globally optimum operating points for a VMD-FPC module with integrated heat recovery by heat pump at varying efficiencies. Additionally, the trend line of the corresponding mean permeate flux J_w in kg m^{-2} h^{-1}, and the daily average electric power demand, which needs to be supplied by a corresponding capacity of PV panels with packs of batteries to tolerate the fluctuation, are calculated and plotted in the Figure 7b.

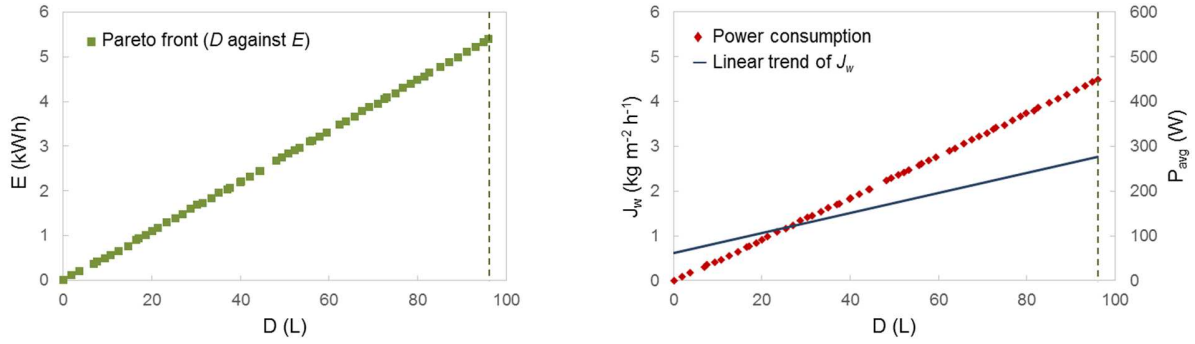

(a) (b)

Figure 7: Global optimization results for VMD-FPC module with integrated heat recovery via heat pump at varying heat recovery level: (a) Pareto front of D and E; (b) the corresponding daily average permeate flux and electric power consumption

Logically, a marked increase in the production of water can be achieved by heat recovery [29], at the expense of an increase in the required electricity. For instance within 12 hours of operation,

for a water production (D) of about 3.7 L, the optimal electricity consumption (E) is about 0.2 kWh; while for D up to 96 L, the minimal E is about 5.4 kWh. The corresponding daily average permeate flux varied a bit and could be as high as 2.7 kg m^{-2} h^{-1} along the Pareto front, which was not in proportion to D due to the variation of module dimensions. Contrarily, E and the daily average electric power consumption are almost in linear relation with D in the optimal set shown in Figure 7a and 7b, which means the SEEC barely varied, maintained between 52 and 60 kWh m^{-3} regardless of the value of D, even up to nearly 100 L. Therefore, the energy consumption of system operation was effectively lowered compared to conventional MD systems, based on the fact that the thermal energy was already supplied by solar energy. Besides, a maximum module surface area (2 × 1.5m) was selected by the optimization at the maximum production of 96 L, which corresponds to a daily productivity of 32 L m^{-2} day^{-1}.

In the composition of E, it should be noted that the compressor work became the main part of power consumption when operating with an integrated heat pump. At the point where D is about 3.7 L and E equals 0.2 kWh, the consumption by the compressor work was 78.0% of the total E, followed by the vacuum pump consumption for 21.8%, leaving an ignorable circulation pump consumption. Similarly, for the point of the maximum production of 96 L, the total compressor work was 4.22 kWh out of the total E of 5.4 kWh, and the total consumption of the vacuum and circulation pump were respectively 1.17 kWh and 0.011 kWh. Indeed, the evaporator of the heat pump condensed the permeate vapor, as described in Section 2.2, and consequently reduced largely the amount of work required by the vacuum pump. Besides, the recirculation pump remained a minor and even negligible consumption, with the exception of co-occurrence of an extreme module slope β (above 60°) and an extreme feed flow Reynolds number (above 8000), which was never the case in the optimal solutions. Therefore, this invariability of SEEC was due to: (i) the fixed heat pump parameters defined in Table 3 and Table A.1, which led to a compressor work nearly proportional to the permeate production; (ii) the vacuum pump consumption, which was incurred by the uncondensed permeate vapor (0.05 of the total permeate), was in proportion with the permeate production as well.

When comparing the present system (integrated heat pump for permeate condensation and heat recovery) with a previous one [29] (without heat recovery and without heat pump integration),

the production can be substantially enhanced together with a significant improvement in the specific electricity consumption from 239 to 52 - 60 kWh m^{-3}. The latter point can be explained by the location of the permeate condenser before the vacuum pump in the new configuration (Figure 1). Thus, the intensive consumption by the vacuum pump in the previous work (VMD-FPC without heat pump integration) is almost removed and replaced by the compressor consumption in the new configuration as proposed in the present study (VMD-FPC with integrated heat pump).

4.3 Benchmark optimization of VMD-FPC at fixed heat recovery levels

In this section, the optimal performance of the combined system (VMD-FPC with heat pump) was studied at fixed heat recovery levels (η_b = {0, 0.2, 0.4, 0.6, 0.8}) for 3000 simulation runs, respectively. As shown in Figure 8, independent optimization studies were conducted per benchmark, and examined separately.

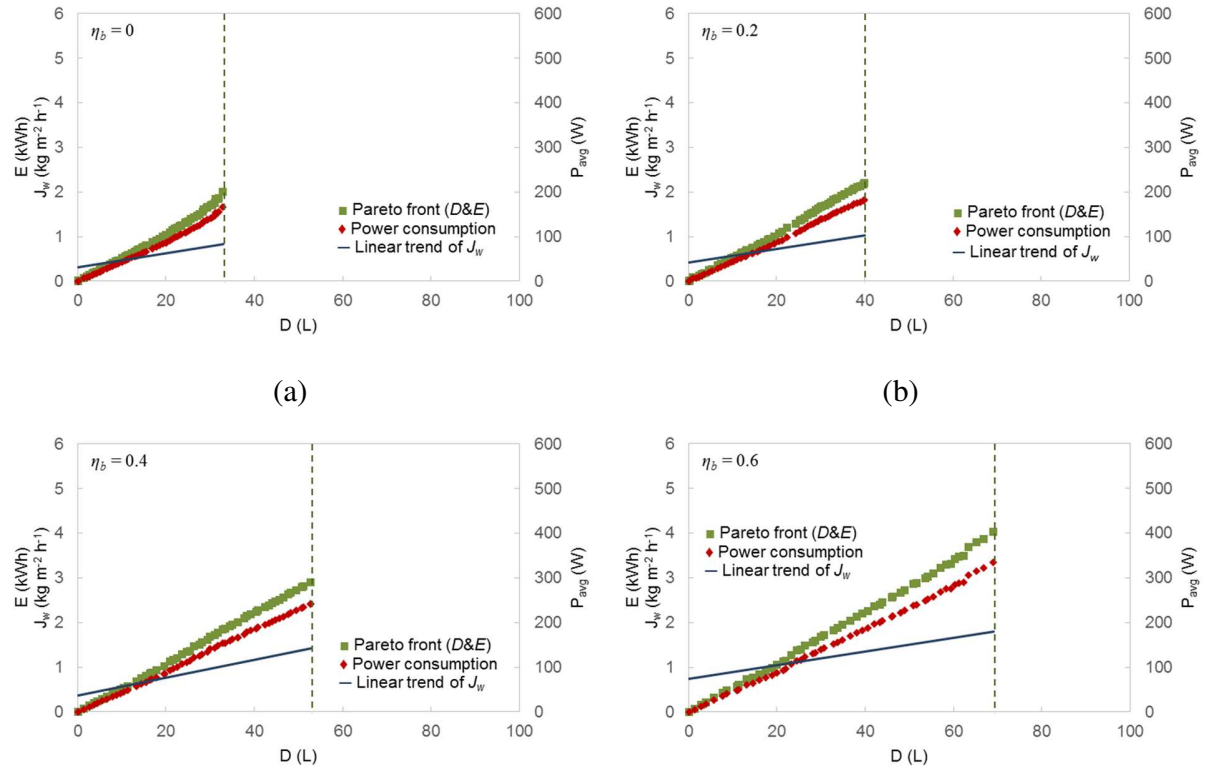

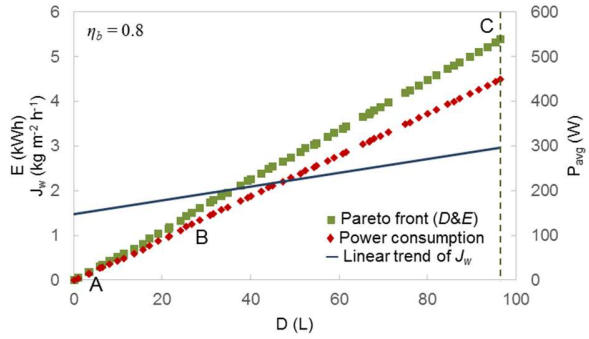

(e)

Figure 8: Pareto fronts (D against E), daily average permeate flux and electric power consumption for the 5 independent optimization benchmarks with fixed heat recovery levels: (a) η_b = 0, (b) η_b = 0.2, (c) η_b = 0.4, (d) η_b = 0.6, (e) η_b = 0.8

Figure 8a shows the optimization with the absence of heat recovery, where the production D is below 32 L and the total consumption E is below 2 kWh. Correspondingly, the daily average permeate flux J_w was limited to be lower than 1 kg m^{-2} h^{-1}. The daily average electric power demand and the total electricity consumption E both increase almost linearly with the production D, resulting in an electric power consumption per unit water production of 4.2 - 5.0 W L^{-1} and an SEEC of 50 - 60 kWh m^{-3}, which is nearly the same as the case in Section 4.2.

Then, from Figure 8a to 8e, a gradual enhancement of maximum D from 32 L to 96 L accumulated during the 12-hour daily operation can be observed with the increment of η_b, where maximum productions of 40 L, 53 L and 70 L were recorded for fixed η_b at 0.2, 0.4 and 0.6, respectively. Similarly, the highest J_w in each benchmark went up from below 1 kg m^{-2} h^{-1} without heat recovery, to 2.8 kg m^{-2} h^{-1} at η_b = 0.8. At the same time, the total consumption E and the average electric power from the installed PV system both kept approximately a linear augmentation with D at a constant slope. As a result, the SEEC and the specific electric power consumption was always in the same ranges as in Figure 8a discussed above.

Therefore, these observations indicate that we can adjust the production capacity of such a system in a certain range according to our demand, without increasing the specific cost if more water is needed. The adjustment can be realized by altering the heat exchanging intensity between the condenser of the heat pump and the feed recirculation: higher η_b can potentially result in higher productivity, but no obvious change in the unit price of the water produced.

In order to better understand the points on the Pareto front, 3 typical points in Figure 8e are chosen to display the detailed variable choices and the performance: Point A, one of the lowest productions on the Pareto front; Point B, an intermediate production (~ 30 L) and consumption (~ 130 W); Point C, the maximums in both D and E. Corresponding variables and performances are summarized in Table 4.

In terms of the solar energy-oriented variables, the 3 points exhibit similar preferences in general. Moreover, these variables were not among the most influential ones, as shown in Figure 5c and 5d. Then in the dimensions, the surface area ($W \times L$) is positively related to the level of water production, while the channel thickness differs among the 3 points. Lastly, among the VMD process variables, the best membrane permeability and the lowest vacuum pressure level were chosen for all 3 points by the optimization. The former is easy to comprehend, while the latter induced lower feed circulation temperature than the cases with higher vacuum pressure under the same amount of thermal power for evaporation, because the same feed temperature level in relatively high vacuum pressure cases cannot be maintained due to the bigger driving force and bigger permeate flux created by the low vacuum pressure of 650 Pa, which demands higher thermal power provision. Thus, the heat exchanging condition in the condenser of the heat pump would be better in lower vacuum pressure condition, which is favored especially in the case with the highest condenser efficiency when heat recovery played a dominant role. On the other hand, the choice of Reynolds number displays the same trend as the width: higher Re with higher production D.

Table 4: Performance analysis over the Pareto front in Figure 8e (three representative operating points: A, B and C)

Variable		A	B	C
Solar thermal collector	n_c	1.44	1.44	1.44
	K (m^{-1})	32	26.4	26.4
	δ_c (mm)	2	2	2
	ε_c	0.845	0.81	0.6
	ε_{ap}	0.695	0.525	0.78
	α_n	0.89	0.89	0.89
	$\beta°$	0	0	0

	$\gamma°$	0	0	-8
Dimensions	W (m)	0.24	0.52	1.5
	δ_f (mm)	21.2	21.2	12.3
	L (m)	0.735	1.81	1.91
VMD process	K_{mref} (s mol$^{1/2}$ m^{-1} kg$^{-1/2}$)	1.85×10^{-5}	1.85×10^{-5}	1.85×10^{-5}
	Re	2400	7500	10000
	P_p (Pa)	650	650	650
Performance				
Water Production	Daily production D (L)	3.7	27.7	96.4
	Average permeate flux (kg m^{-2} h^{-1})	1.7	2.4	2.8
Electrical Consumption (PV panels)	Total electricity E (kWh)	0.21	1.55	5.38
	Circulation pump (kWh)	4.06×10^{-6}	2.99×10^{-4}	8.93×10^{-3}
	Vacuum pump (kWh)	0.04	0.33	1.16
	Compressor work (kWh)	0.16	1.21	4.21
	SEEC (kWh m^{-3})	55.91	55.81	55.83
	Average power demand (W)	17.3	128.8	448.7
	Estimated area of PV panel (m^2)	0.13	0.95	3.26
Solar thermal energy utilized (kWh)		0.96	5.21	15.26

Different production levels were selected for these 3 points: 3.7 L, 27.7 L, and the maximum 96.4 L. Meanwhile, the total consumption E and power demand are directly in proportion to the production, which indicates that bigger installed PV capacity is required for higher demand of water productivity. The most common size of a PV panel is 1.6 m^2 with a power capacity of around 220W [51], based on which the area of the PV panel can be estimated in Table 4. The composition of the E was the same as discussed in Section 4.2, and the solar thermal energy utilized was bigger with larger module surfaces. Therefore, according to our calculations of Point B in the middle, a daily amount of nearly 28 L, corresponding to the drinking water quantity required for a small community of 10-15 persons, could be autonomously produced on the sunny day of 1st August at Toulouse, assisted by a PV system with a dedicated power capacity of about 130 W, corresponding to a PV panel area of 0.95 m^2. The size of the integrated module at Point B was 0.94 m^2, which took into account the surface area of both the solar thermal collector and the membrane. Correspondingly, the daily production capacity in terms of per unit surface area of this small membrane distillation equipment was 29.4 L m^{-2} at Point B. In the literature of small-scale solar-driven MD reviewed in Section 1.2, this value has barely reached 10 L m^{-2} regardless

of the system configuration. For instance, in a recent case of a FPC-powered DCMD system with a total solar collector area of 2.61 m^2 and a total membrane area of 1 m^2, the maximum daily production capacity was calculated to be 9.3 L m^{-2} [22]. On the other hand, the STEC at Point B considering the utilized solar energy was 188 kWh m^{-3}, which is comparable to the lowest thermal SECs in Table 1. Besides, the constant SEEC level of around 55 kWh m^{-3} is also lower than the reported range of 200 - 300 kWh m^{-3} in a few references [23,29,31], though not widely discussed in the literature. Conclusively, the equipment developed in this work can largely augment the production capacity per unit surface area of solar-powered MD system with relatively low energy consumption, which adds to its applicability to small-scale domestic desalination devices in remote areas.

In addition, the dynamic accumulations of D and E during the operation of the point B are presented in Figure 9, as well as the variation of the solar radiation intensity received (G_T) on the module surface and the intensity absorbed by the module (G_S). Although solar condition has varied drastically during the operation, freshwater could be produced at a fairly steady pace, with total consumption increasing steadily. As a result, the integration of the heat pump has not only improved water productivity, but also buffered the fluctuation of solar radiation.

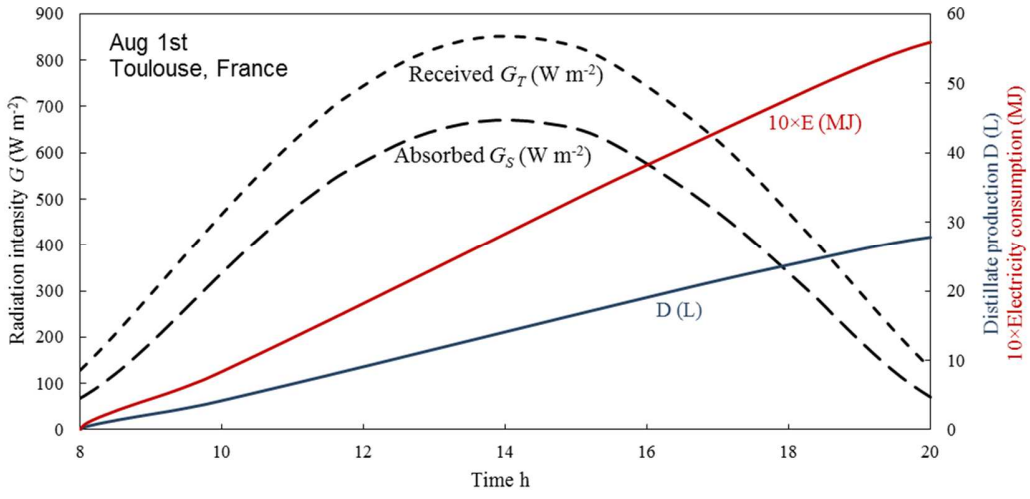

Figure 9: Dynamic variations of solar radiation intensities, accumulated distillate production and accumulated electricity consumption of Point B in Figure 8e

4.4 Pareto-based study of decision variables and key indications on design

Here, the globally optimal decision variables are classified into 3 groups: (i) solar energy-oriented variables, (ii) VMD process variables, and (iii) module dimensions. The range of each decision variable in the optimal Pareto front, i.e. at its optimal values, is summarized, presented and discussed in this section. In addition to the optimal range of variables, the median values were also accounted, to be representative and to give a better idea of a typical value without being distorted by extremely large or small values across the Pareto set.

4.4.1 Solar energy-oriented variables

8 variables belong to this group, namely the slope $\beta°$ and the azimuth angle $\gamma°$ of VMD-FPC collector, the refractive index n_c, the extinction coefficient K (m^{-1}), the thickness δ_c (m) and the emittance ε_c of the glazing cover, the emittance ε_{ap} and the absorptance α_n in the normal direction of the absorber-plate. All median values and ranges of these variables are shown in Figure 10.

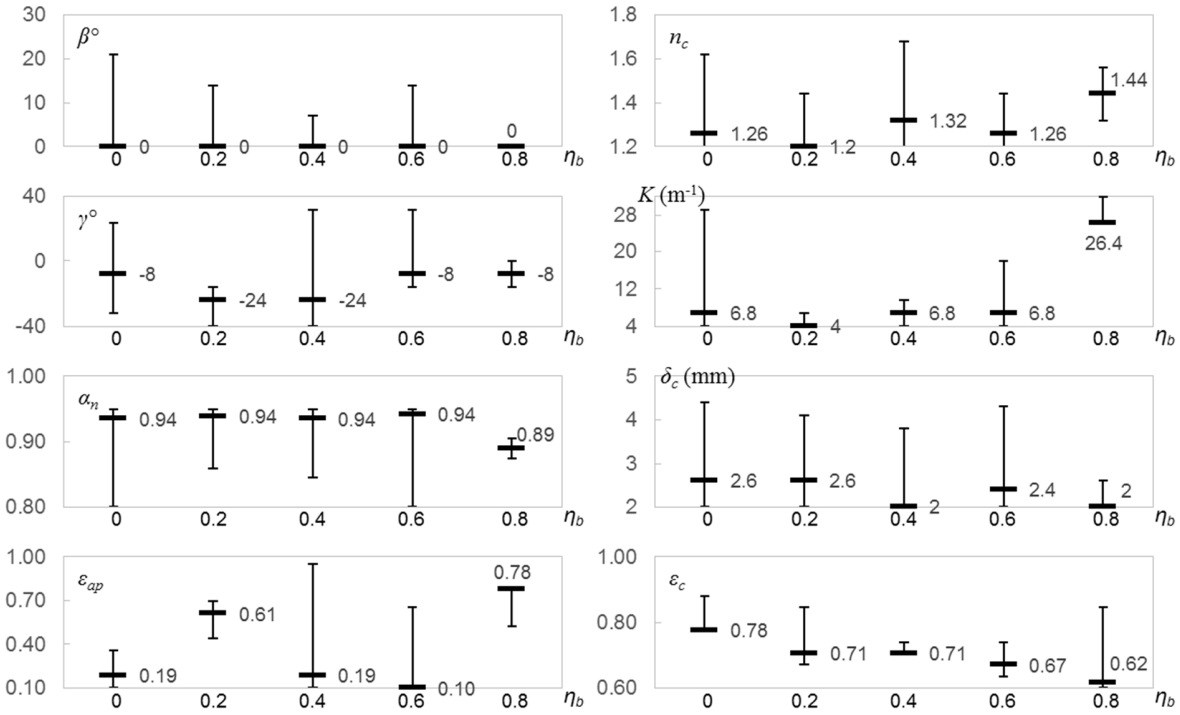

Figure 10: Ranges and typical values of optimal solar energy-oriented variables at different η_b

741 The slope β of the module has an impact on the received solar energy and on the energy
742 consumption of the recirculation pump. For the former, a slightly sloped surface benefits the
743 exposure to solar radiation. While for the latter, the inclination of the module increases the
744 burden of the recirculation pump. The preferred value of β are typically 0 (no slope) no matter
745 the level of heat recovery, but its varying range in the optimal set generally shows a downward
746 trend with higher heat recovery, which implies that when the heat recovery rate is high, the direct
747 solar radiation and absorption becomes less important and the system favors a less inclined
748 surface to reduce the power consumption. On the other hand, the optimal values of the azimuth
749 angle indicated that the collector preferred to be placed a bit to the east (negative value), and not
750 directly to the south. This can be explained by the daily operating time, which was from 8 am to 8
751 pm with daylight saving in France (1 hour in advance). Hence, the sun was still in the east at
752 12:00 in local time, instead of at an azimuth angle of zero. Therefore, placing the collector
753 slightly to the east can benefit the reception of solar radiation during the operating time.
754 Normally for an all-day operation from sunrise to sunset, the collectors are placed right to the
755 south ($\gamma = 0°$) to maximize the solar absorption.
756
757 Higher values of α_n and lower values of ε_{ap} of the absorber-plate are more preferable to enhance
758 the solar energy absorbed by the module, as also detected by the AMOEA-MAP for most of the
759 five benchmarks with different condenser efficiencies. Abnormalities of a little lower α_n and a
760 higher ε_{ap} were witnessed especially at the highest heat recovery level, which was probably due
761 to the lower dependence of the system performance on the solar energy resource when heat
762 recovery was intensive. Besides, an intermediate value of ε_{ap} of the absorber-plate (0.4 to 0.7)
763 was chosen to be the optimal in the low heat recovery level (η_b = 0.2), allowing a higher loss
764 coefficient from the top of the collector. This possibly indicates that the feed operating
765 temperatures in this optimal set were not far from the ambient based on its vacuum pressure level
766 (will be seen in Section 4.4.2), thus the top loss was already little, which might need further
767 observations with more simulations.
768
769 Generally, lower values of n_c, K, and δ_c of the glass cover are more preferable to optimize the
770 amount of solar energy that penetrates through the cover and gets to the absorber-plate.
771 Nonetheless, the preferences for n_c and K were less demanded when highest heat recovery came

into play, especially at η_b = 0.8, as shown in Figure 10. The same interpretation might account for this change, as the amount of solar energy absorbed by the system was lower with a higher level of heat recovery. Regarding the glass emittance ε_c, the tendency of optimal choices decreases slightly with increasing condenser efficiency, indicating that the system preferred the glass cover to store more radiation energy in itself when the heat recovery level was lower.

4.4.2 VMD process variables

The membrane permeability at the reference temperature of 20°C (K_{mref} in s mol$^{1/2}$ m^{-1} kg$^{-1/2}$), the permeate vacuum pressure (P_p in Pa), and the Reynolds number are the 3 VMD process variables studied in the present work. Their optimal ranges and median values are shown in Figure 11.

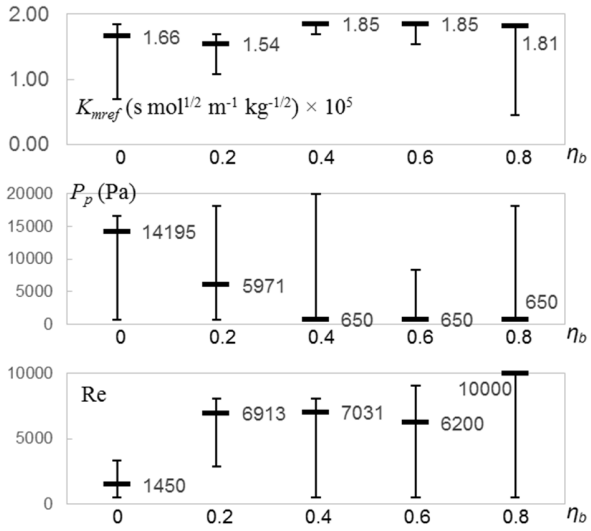

Figure 11: Ranges and typical values of optimal VMD process variables at different η_b

Membranes with better permeability were undoubtedly appreciated in all benchmarks, and the optimal value of K_{mref} was further pushed to the highest (1.85 × 10^{-5} s mol$^{1/2}$ m^{-1} kg$^{-1/2}$) in higher heat recovery levels ($\eta_b \geq 0.4$) when the constraint from solar energy absorption became less significant and the mass transfer quality turned out more important.

As one of the most influential variables as discussed in Section 4.1, the vacuum pressure P_p varied a lot in all benchmarks. However, a gradual change of preference is observable in the

figures, from low (η_b = 0 and 0.2) to high heat recovery levels (η_b = 0.4, 0.6 and 0.8). In the former cases, the water productivity of the system was more limited by the absorbed solar energy, thus an extreme low vacuum pressure would not be favorable because it only added to E by higher consumption of the vacuum pump and was not capable of largely enhancing D. Consequently, intermediate values were found by the optimization to balance D and E: 14 195 Pa for no heat recovery and 5 971 Pa for η_b = 0.2, and the latter value is lower due to the less restraining thermal energy income by a little bit of heat recovery. Therefore, lower optimal vacuum pressure can be achieved when heat recovery started to be included. This became even more obvious in the cases of η_b > 0.2, where the lowest vacuum pressure was often selected in the optimization. Correspondingly, higher productions with higher thermal energy demands were able to be attained with the help of relatively high condenser efficiencies in the heat pump.

Higher Reynolds numbers are beneficial to the heat and mass transfer from the feed bulk to the membrane surface, reducing the thermal and concentration polarizations and strengthening the permeate flux. With regards to the first benchmark, i.e. the system without heat recovery, the optimum value of Re proved to be 1 450 (laminar regime). Here, lower Re values were preferred because of the connection between the recirculation pump consumption and the flow rate, where an optimal value has been found by balancing energy consumption and water production, which was again limited by solar energy, same as explained in the choice of vacuum pressure. Then, the optimal option of the flow regime of the feed recirculation became totally turbulent and was even pushed up to the maximum of 10 000 at η_b = 0.8, in order to fully explore the maximum water production despite the elevated consumption by the circulation pump, because it became comparatively ignorable in this benchmark, as presented by the data of the Points A, B and C.

4.4.3 Dimension variables

In Figure 12, the optimum dimensions of the feed channel, i.e. the width W (m), the thickness δ_f (m) and the length L (m) are illustrated.

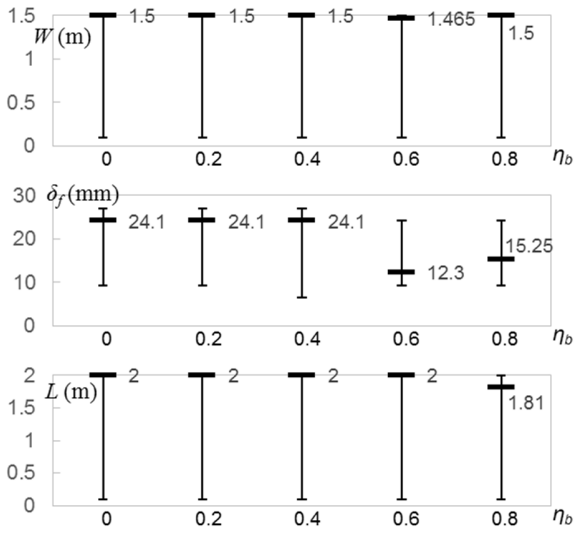

Figure 12: Ranges and typical values of dimension variables at different η_b

Among them, W and L possessed great importance to the objectives, as discussed in Section 4.1. Therefore, the collector surface A_c tended to vary between the smallest (0.1m × 0.1m) and the largest (1.5m × 2m) in all benchmarks, shaping up the Pareto fronts (Figure 7 and Figure 8) of the total production D and the total energy consumption E after the 12h operation. Despite the dispersion, a larger surface area was apparently more favored, as shown by the median values in the figure, to obtain the highest possible productivity of the module. However, in the design for applications, one may only have to simply fix an appropriate surface dimension according to the freshwater demand. The electric consumption and the PV capacity to be installed would directly depend on the level of water production based on the linear relation between D and E, as discussed in Section 4.3.

At a certain Re number, the velocity of the feed flow is lower when the characteristic length of the flow channel is bigger, which results in a decrease in the quality of mass transfer due to a stronger temperature and concentration polarization. In that sense, the thickness of the flow channel (δ_f) is a much more determining factor of the characteristic length with respect to the width W, on account that it is much smaller than the other. However, the typical value found by the optimizations was a middle value, not at the lower limit of 0.5mm with the highest feed flow velocity for a given Reynolds number. Indeed, the energy consumption of the recirculation pump increases sharply with the increment in flow velocity, it is therefore necessary to find a balance

by adjusting the thickness of the flow channel, which could also have some technical limitations. From no heat recovery to intermediate heat recovery (η_b = 0, 0.2 and 0.4) where water production was relatively more restrained by incoming solar energy, the balances found by the optimization were closer to the upper boundary of the variable defined in Table 2 (30mm), implying that it was more important to limit the pumping consumption than to enhance the flow rate and ameliorate the mass transfer quality. While for higher heat recovery levels (η_b = 0.6 and 0.8) where the thermal demand for solar energy became less with the help of more efficient heat recovery, lower δ_f values were selected and the balance moved a bit to the opposite direction compared to the other benchmarks.

5 Conclusions and perspectives

On the basis of a small-scale integrated vacuum membrane distillation - flat plate collector (VMD-FPC) module previously studied, a simultaneous strategy of heat recovery and permeate condensation by a heat pump was proposed, studied and optimized, aiming domestic applications in remote coastal areas or isolated islands. The heat pump unit proposed in this work was capable of both recovering the latent heat of evaporation and offering a practical condensation strategy before the vacuum pump, exempting the use of additional intensive cooling and the excessive burden on the vacuum pump. The VMD-FPC module with integrated heat pump allowed indeed for a substantial gain in terms of water production with relatively low solar thermal energy and PV electricity consumption. Under a rather high heat recovery regime, the optimal results for different scales of production revealed that, for a cloudless 12-hour operation on Aug 1st in Toulouse, France, the water production could largely range from 3.7 L up to 96 L with corresponding electric power consumptions equal to 17 W (~ 0.13 m^2 of PV panel) and 449 W (~ 3.26 m^2 of PV panel), respectively. Interestingly, for all simulations, the need for PV power capacity per unit water production was reported to be almost constant ranging in 4.2 - 5.0 W L^{-1}, which corresponds to a PV area of 0.031 - 0.036 m^2 L^{-1}.

Besides, the process efficiency and the significance of design and operating variables were investigated by global sensitivity analyses (SA) and by several design-oriented multi-objective optimizations. In the SAs, the VMD process variables, such as Reynolds number and membrane permeability, gained more impact on the performance of the system when heat recovery included.

In the optimizations, a detailed study of the Pareto fronts at different heat recovery levels made it possible to provide several indications on the optimal operation of the system. Logically, the optimization of a VMD-FPC module without heat recovery leads to an improvement of the solar absorption by adjusting the solar-oriented variables. While in the case of being equipped with an intensive heat recovery system, the overall performance of the module is less sensitive to solar-oriented variables. Regarding the VMD variables, high membrane permeability is always welcome, while high Reynolds number, which decides the hydrodynamic condition of the feed compartment, is only to choose for elevated water production scales, i.e. an integrated module with intensive heat recovery level. Finally, the channel thickness should be increased if the heat recovery efficiency is low, and the surface area of the module determines the scale of production, which needs to be decided according to the actual demand and the maximum installed PV capacity limited by economic criteria and other logistic constraints for a given application.

Based on the promising results discussed in this work, a prototype in our laboratory is expected in the near future to confirm the technical feasibility of such a concept equipment. Further, lower consumption could also be anticipated by applying advanced heat pumps and reusing excess power.

Acknowledgment

This work was supported by the ANR (Agence Nationale de la Recherche) project: LabCom - Membranes pour le traitement d'eaux des Océans avec énergie Solaire en régions Tropicales (MOST), 2018; and China Scholarship Council (CSC) [No. 201504490023], 2015.

Declarations of interest: None.

References

[1] P. Jacob, S. Laborie, C. Cabassud, Visualizing and evaluating wetting in membrane distillation: New methodology and indicators based on Detection of Dissolved Tracer Intrusion (DDTI), Desalination. 443 (2018) 307–322. https://doi.org/10.1016/j.desal.2018.06.006.

[2] E. Guillén-Burrieza, J. Blanco, G. Zaragoza, D.-C. Alarcón, P. Palenzuela, M. Ibarra, W. Gernjak, Experimental analysis of an air gap membrane distillation solar desalination pilot system, Journal of Membrane Science. 379 (2011) 386–396. https://doi.org/10.1016/j.memsci.2011.06.009.

[3] N. Ghaffour, T.M. Missimer, G.L. Amy, Technical review and evaluation of the economics of water desalination: Current and future challenges for better water supply sustainability, Desalination. 309 (2013) 197–207. https://doi.org/10.1016/j.desal.2012.10.015.
[4] K.W. Lawson, D.R. Lloyd, Membrane distillation, Journal of Membrane Science. 124 (1997) 1–25. https://doi.org/10.1016/S0376-7388(96)00236-0.
[5] J.-P. Mericq, S. Laborie, C. Cabassud, Vacuum membrane distillation for an integrated seawater desalination process, Desalination and Water Treatment. 9 (2009) 287–296. https://doi.org/10.5004/dwt.2009.862.
[6] N. Thomas, M.O. Mavukkandy, S. Loutatidou, H.A. Arafat, Membrane distillation research & implementation: Lessons from the past five decades, Separation and Purification Technology. 189 (2017) 108–127. https://doi.org/10.1016/j.seppur.2017.07.069.
[7] M. Khayet, Membranes and theoretical modeling of membrane distillation: A review, Advances in Colloid and Interface Science. 164 (2011) 56–88. https://doi.org/10.1016/j.cis.2010.09.005.
[8] A. Alkhudhiri, N. Darwish, N. Hilal, Membrane distillation: A comprehensive review, Desalination. 287 (2012) 2–18. https://doi.org/10.1016/j.desal.2011.08.027.
[9] A.C. Sun, W. Kosar, Y. Zhang, X. Feng, Vacuum membrane distillation for desalination of water using hollow fiber membranes, Journal of Membrane Science. 455 (2014) 131–142. https://doi.org/10.1016/j.memsci.2013.12.055.
[10] J.-P. Mericq, S. Laborie, C. Cabassud, Evaluation of systems coupling vacuum membrane distillation and solar energy for seawater desalination, Chemical Engineering Journal. 166 (2011) 596–606. https://doi.org/10.1016/j.cej.2010.11.030.
[11] A. Deshmukh, C. Boo, V. Karanikola, S. Lin, A.P. Straub, T. Tong, D.M. Warsinger, M. Elimelech, Membrane Distillation at the Water-Energy Nexus: Limits, Opportunities, and Challenges, Energy Environ. Sci. (2018). https://doi.org/10.1039/C8EE00291F.
[12] R. Miladi, N. Frikha, S. Gabsi, Exergy analysis of a solar-powered vacuum membrane distillation unit using two models, Energy. 120 (2017) 872–883. https://doi.org/10.1016/j.energy.2016.11.133.
[13] K. Manzoor, S.J. Khan, Y. Jamal, M.A. Shahzad, Heat extraction and brine management from salinity gradient solar pond and membrane distillation, Chemical Engineering Research and Design. 118 (2017) 226–237. https://doi.org/10.1016/j.cherd.2016.12.017.
[14] P.A. Hogan, Sudjito, A.G. Fane, G.L. Morrison, Desalination by solar heated membrane distillation, Desalination. 81 (1991) 81–90. https://doi.org/10.1016/0011-9164(91)85047-X.
[15] Z. Ding, L. Liu, M.S. El-Bourawi, R. Ma, Analysis of a solar-powered membrane distillation system, Desalination. 172 (2005) 27–40. https://doi.org/10.1016/j.desal.2004.06.195.
[16] H.C. Duong, L. Xia, Z. Ma, P. Cooper, W. Ela, L.D. Nghiem, Assessing the performance of solar thermal driven membrane distillation for seawater desalination by computer simulation, Journal of Membrane Science. 542 (2017) 133–142. https://doi.org/10.1016/j.memsci.2017.08.007.
[17] H. Chang, S.-G. Lyu, C.-M. Tsai, Y.-H. Chen, T.-W. Cheng, Y.-H. Chou, Experimental and simulation study of a solar thermal driven membrane distillation desalination process, Desalination. 286 (2012) 400–411. https://doi.org/10.1016/j.desal.2011.11.057.
[18] S.E. Moore, S.D. Mirchandani, V. Karanikola, T.M. Nenoff, R.G. Arnold, A. Eduardo Sáez, Process modeling for economic optimization of a solar driven sweeping gas membrane distillation desalination system, Desalination. 437 (2018) 108–120. https://doi.org/10.1016/j.desal.2018.03.005.

955 [19] F. Banat, N. Jwaied, M. Rommel, J. Koschikowski, M. Wieghaus, Desalination by a
956 “compact SMADES” autonomous solarpowered membrane distillation unit, Desalination.
957 217 (2007) 29–37. https://doi.org/10.1016/j.desal.2006.11.028.
958 [20] H.E.S. Fath, S.M. Elsherbiny, A.A. Hassan, M. Rommel, M. Wieghaus, J. Koschikowski, M.
959 Vatansever, PV and thermally driven small-scale, stand-alone solar desalination systems
960 with very low maintenance needs, Desalination. 225 (2008) 58–69.
961 https://doi.org/10.1016/j.desal.2006.11.029.
962 [21] S.T. Bouguecha, S.E. Aly, M.H. Al-Beirutty, M.M. Hamdi, A. Boubakri, Solar driven
963 DCMD: Performance evaluation and thermal energy efficiency, Chemical Engineering
964 Research and Design. 100 (2015) 331–340. https://doi.org/10.1016/j.cherd.2015.05.044.
965 [22] A.E. Kabeel, M. Abdelgaied, E.M.S. El-Said, Study of a solar-driven membrane distillation
966 system: Evaporative cooling effect on performance enhancement, Renewable Energy. 106
967 (2017) 192–200. https://doi.org/10.1016/j.renene.2017.01.030.
968 [23] X. Wang, L. Zhang, H. Yang, H. Chen, Feasibility research of potable water production via
969 solar-heated hollow fiber membrane distillation system, Desalination. 247 (2009) 403–411.
970 https://doi.org/10.1016/j.desal.2008.10.008.
971 [24] Y. Wang, Z. Xu, N. Lior, H. Zeng, An experimental study of solar thermal vacuum
972 membrane distillation desalination, Desalination and Water Treatment. 53 (2015) 887–897.
973 https://doi.org/10.1080/19443994.2014.927187.
974 [25] K. Murase, Y. Yamagishi, K. Tano, Development of a hybrid solar distillator of a basin type
975 distillator and a membrane distillator, Desalination and Water Treatment. 9 (2009) 96–104.
976 https://doi.org/10.5004/dwt.2009.757.
977 [26] T.-C. Chen, C.-D. Ho, Immediate assisted solar direct contact membrane distillation in
978 saline water desalination, Journal of Membrane Science. 358 (2010) 122–130.
979 https://doi.org/10.1016/j.memsci.2010.04.037.
980 [27] H. Chang, C.-L. Chang, C.-D. Ho, C.-C. Li, P.-H. Wang, Experimental and simulation study
981 of an air gap membrane distillation module with solar absorption function for desalination,
982 Desalination and Water Treatment. 25 (2011) 251–258.
983 https://doi.org/10.5004/dwt.2011.1880.
984 [28] C.-D. Ho, C.A. Ng, P.-H. Wang, C.-H. Cheng, Theoretical and experimental studies of
985 immediate assisted solar air gap membrane distillation systems, Desalination and Water
986 Treatment. 57 (2016) 3846–3860. https://doi.org/10.1080/19443994.2014.989274.
987 [29] Q. Ma, A. Ahmadi, C. Cabassud, Direct integration of a vacuum membrane distillation
988 module within a solar collector for small-scale units adapted to seawater desalination in
989 remote places: Design, modeling & evaluation of a flat-plate equipment, Journal of
990 Membrane Science. 564 (2018) 617–633. https://doi.org/10.1016/j.memsci.2018.07.067.
991 [30] S.B. Abdallah, N. Frikha, S. Gabsi, Study of the performances of different configurations of
992 seawater desalination with a solar membrane distillation, Desalination and Water Treatment.
993 52 (2014) 2362–2371. https://doi.org/10.1080/19443994.2013.792746.
994 [31] Q. Li, L.-J. Beier, J. Tan, C. Brown, B. Lian, W. Zhong, Y. Wang, C. Ji, P. Dai, T. Li, P. Le
995 Clech, H. Tyagi, X. Liu, G. Leslie, R.A. Taylor, An integrated, solar-driven membrane
996 distillation system for water purification and energy generation, Applied Energy. 237 (2019)
997 534–548. https://doi.org/10.1016/j.apenergy.2018.12.069.
998 [32] M. Khayet, Solar desalination by membrane distillation: Dispersion in energy consumption
999 analysis and water production costs (a review), Desalination. 308 (2013) 89–101.
1000 https://doi.org/10.1016/j.desal.2012.07.010.

[33] J.-P. Mericq, S. Laborie, C. Cabassud, Vacuum membrane distillation of seawater reverse osmosis brines, Water Research. 44 (2010) 5260–5273. https://doi.org/10.1016/j.watres.2010.06.052.
[34] J.A. Duffie, W.A. Beckman, Solar engineering of thermal processes, Wiley New York, 2013.
[35] J.I. Mengual, M. Khayet, M.P. Godino, Heat and mass transfer in vacuum membrane distillation, International Journal of Heat and Mass Transfer. 47 (2004) 865–875. https://doi.org/10.1016/j.ijheatmasstransfer.2002.09.001.
[36] J.-P. Mericq, Approche intégrée du dessalement d'eau de mer: Distillation membranaire sous vide pour la réduction des rejets salins et possibilités de couplage avec l'énergie solaire, 2009. http://eprint.insa-toulouse.fr/archive/00000341/ (accessed February 12, 2016).
[37] E.N. Sieder, G.E. Tate, Heat transfer and pressure drop of liquids in tubes, Industrial & Engineering Chemistry. 28 (1936) 1429–1435.
[38] V. Gnielinski, New equations for heat and mass-transfer in turbulent pipe and channel flow, International Chemical Engineering. 16 (1976) 359–368.
[39] T.L. Bergman, F.P. Incropera, Fundamentals of heat and mass transfer, John Wiley & Sons, 2011.
[40] D.T. Jamieson, J.S. Tudhope, R. Morris, G. Cartwright, Physical properties of sea water solutions: heat capacity, Desalination. 7 (1969) 23–30. https://doi.org/10.1016/S0011-9164(00)80271-4.
[41] L. Yuan-Hui, S. Gregory, Diffusion of ions in sea water and in deep-sea sediments, Geochimica et Cosmochimica Acta. 38 (1974) 703–714. https://doi.org/10.1016/0016-7037(74)90145-8.
[42] scipy.integrate.ode — SciPy v0.18.1 Reference Guide, (n.d.). https://docs.scipy.org/doc/scipy-0.18.1/reference/generated/scipy.integrate.ode.html (accessed December 14, 2017).
[43] A. Desideri, S. Gusev, M. van den Broek, V. Lemort, S. Quoilin, Experimental comparison of organic fluids for low temperature ORC (organic Rankine cycle) systems for waste heat recovery applications, Energy. 97 (2016) 460–469. https://doi.org/10.1016/j.energy.2015.12.012.
[44] R. Andrzejczyk, T. Muszyński, The performance of H2O, R134a, SES36, ethanol, and HFE7100 two-phase closed thermosyphons for varying operating parameters and geometry, Archives of Thermodynamics. 38 (2017) 3–21. https://doi.org/10.1515/aoter-2017-0013.
[45] J. Herman, W. Usher, SALib: an open-source Python library for sensitivity analysis, The Journal of Open Source Software. 2 (2017).
[46] E. Borgonovo, A new uncertainty importance measure, Reliability Engineering & System Safety. 92 (2007) 771–784. https://doi.org/10.1016/j.ress.2006.04.015.
[47] E. Plischke, E. Borgonovo, C.L. Smith, Global sensitivity measures from given data, European Journal of Operational Research. 226 (2013) 536–550. https://doi.org/10.1016/j.ejor.2012.11.047.
[48] A. Saltelli, Sensitivity analysis for importance assessment, Risk Analysis. 22 (2002) 579–590.
[49] A. Ahmadi, L. Tiruta-Barna, F. Capitanescu, E. Benetto, A. Marvuglia, An archive-based multi-objective evolutionary algorithm with adaptive search space partitioning to deal with expensive optimization problems: Application to process eco-design, Computers & Chemical Engineering. 87 (2016) 95–110. https://doi.org/10.1016/j.compchemeng.2015.12.008.

[50] A. Ahmadi, Memory-based adaptive partitioning (MAP) of search space for the enhancement of convergence in Pareto-based multi-objective evolutionary algorithms, Applied Soft Computing. 41 (2016) 400–417. https://doi.org/10.1016/j.asoc.2016.01.029.
[51] Solar panels, Energy Saving Trust. (n.d.). https://www.energysavingtrust.org.uk/renewable-energy/electricity/solar-panels (accessed February 15, 2019).

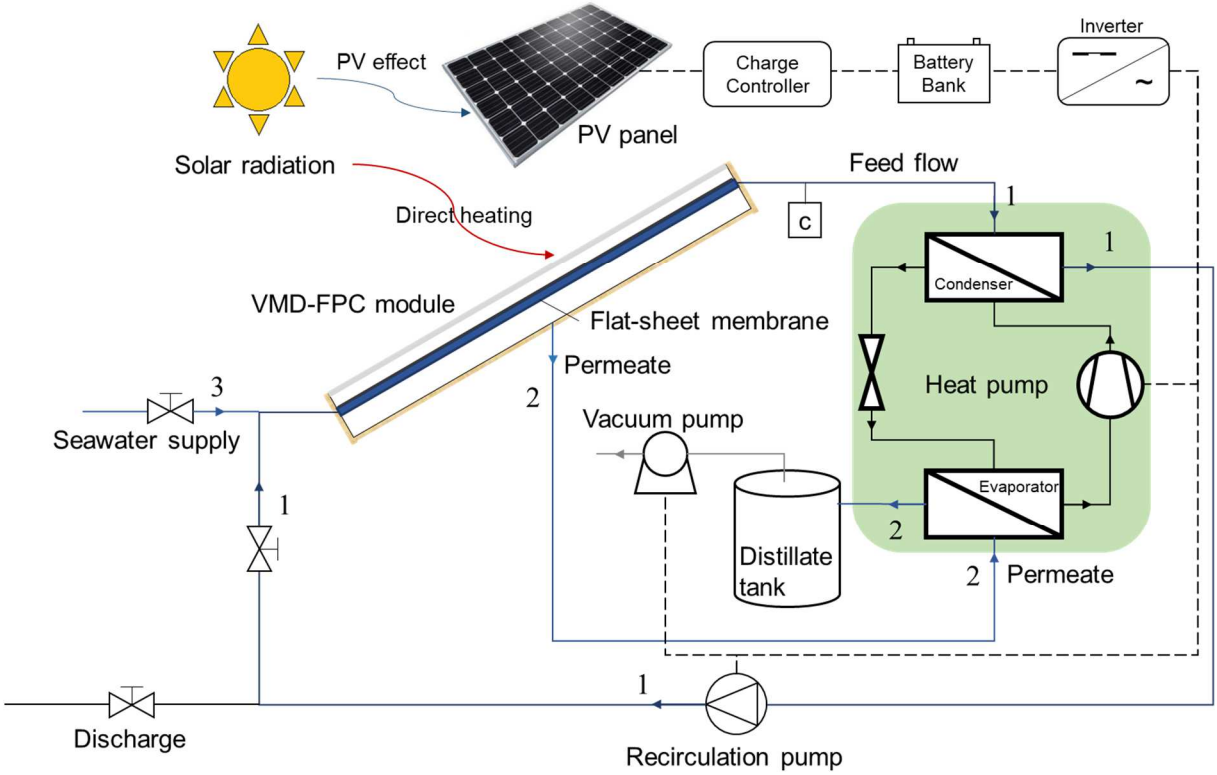
PV effect
PV panel
Charge Controller
Battery Bank
Inverter
Solar radiation
Direct heating
Feed flow
C
1
Condenser
1
VMD-FPC module
Flat-sheet membrane
Permeate
2
Heat pump
3
Seawater supply
Vacuum pump
Evaporator
1
2
Distillate tank
2
Permeate
1
Discharge
1
Recirculation pump